Solid State Communications 360 (2023) 115051

Contents lists available at ScienceDirect

Solid State Communications

journal homepage: www.elsevier.com/locate/ssc

Synthesis, crystal structure, and superconductivity of Ba$(Bi_{0.25}Pb_{0.75})_{1-x}Mg_xO_{3-\delta}$

Xiande Zheng [c], Muhammad Asim Farid [b], Xiaoge Wang [a], Yan Wang [a], Jinling Geng [a], Fuhui Liao [a], Junliang Sun [a], Guobao Li [a,*], Laijun Liu [c,**], Jianhua Lin [a,***]

[a] Beijing National Laboratory for Molecular Sciences, State Key Laboratory of Rare Earth Materials Chemistry and Applications, College of Chemistry and Molecular Engineering, Peking University, Beijing, 100871, People's Republic of China
[b] Department of Chemistry, Division of Science and Technology, University of Education, Lahore, Pakistan
[c] College of Materials Science and Engineering, Guilin University of Technology, Guilin, 541004, People's Republic of China

ARTICLE INFO

Communicated by Zhao Liuyan

Keywords:
Solid-state reaction
Superconductivity
Perovskite
Structure
$Ba(Bi_{0.25}Pb_{0.75})_{1-x}Mg_xO_{3-\delta}$

ABSTRACT

Magnesium has been doped into the B-site of $BaBi_{0.25}Pb_{0.75}O_{3-\delta}$ to form a solid solution Ba$(Bi_{0.25}Pb_{0.75})_{1-x}Mg_xO_{3-\delta}$ ($0 \le x \le 0.10$) by solid-state reaction. The X-ray, neutron, and selected area electron diffraction are used to confirm that this solid solution crystallizes in triclinic space group $P1$. The unit cell volume of Ba$(Bi_{0.25}Pb_{0.75})_{1-x}Mg_xO_{3-\delta}$ increases with Mg, which is surprising because the radius of Mg^{2+} is smaller than any radius of Bi^{3+}, Bi^{5+}, Pb^{2+}, and Pb^{4+}. XPS and iodometric titration data of samples show that the oxygen vacancies increase with Mg in Ba$(Bi_{0.25}Pb_{0.75})_{1-x}Mg_xO_{3-\delta}$. The increased oxygen vacancies result in increase of Bi^{3+}:Bi^{5+} and Pb^{2+}:Pb^{4+} ratios, which is the utmost possible reason for unit cell volume increase. They are all superconductors with T_C^{zero} (the highest temperature at which the electrical resistivity becomes "zero") between 11.2 and 9.2 K.

1. Introduction

Superconductors are magical materials with promising applications based on the perfect diamagnetism and practical zero resistivity in their superconducting state. They have been widely used as electromagnets in MRI/NMR machines [1], mass spectrometers [2], particle accelerators [3], and some tokamaks [4]. They are also promising in high-performance smart grid [5], electric power transmission [6], transformers [7], power storage devices [7], electric motors [8], magnetic levitation devices [9], fault current limiters [10], and superconducting magnetic refrigeration [11]. Finding a new superconductor or improving the properties of a known superconductor is something exciting. The finding of a room-temperature superconductor [12] is very exhilarating. It is still exciting to find superconductivity in magic-angle graphene ($T_C \sim 1.7$ K) [13], a nearly ferromagnetic spin-triplet UTe_2 ($T_C \sim 1.6$ K) [14], and an infinite-layer nickelate $Nd_{0.8}Sr_{0.2}NiO_2$ ($T_C \sim 10.8$ K) [15]. The improvement of superconductivity in $LnFeAsO_{1-x}F_x$ by changing La to Sm (T_C changing from 26 K for $LaFeAsO_{1-x}F_x$ to 43 K for $SmFeAsO_{1-x}F_x$) [16] is also very striking. Many well-known superconductors are layered compounds with strong anisotropic superconductivity, such as $LnBa_2Cu_3O_{7-\delta}$ [17,18], MgB_2 [19,20], $LaFeAsO_{1-x}F_x$ [21], $A_{1-x}Fe_{2-y}Se_2$ (A = K, Cs, Rb, Tl) [22], and so on. This anisotropy is not helpful for the use of the corresponding superconductors. The finding of an isotropic superconductor with $T_C > 40$ K is significant [23]. In fact, the isotropic superconductors are not too less, which include the most element superconductors [24], many alloy superconductors [24], $BaBiO_3$-based superconductors, the recent reported hydrogen-rich materials under high pressure such as H_3S [25] and LaH_{10} [26]. Although room temperature superconductivity has already been found in hydrogen-rich materials [12], the high pressure needed hinders their wide application. More efforts are needed to find new isotropic superconductors, or to improve the existing isotropic superconductors. $BaBiO_3$-based material showing the highest T_C at normal pressure in the isotropic superconductors is one of the promising candidates for modification. Therefore, since the reports of superconductivity in $BaBi_{1-y}Pb_yO_{3-\delta}$ [27] and $Ba_{1-x}K_xBiO_3$ [28], $BaBiO_3$ based

* Corresponding author.
** Corresponding author.
*** Corresponding author.
E-mail addresses: liguobao@pku.edu.cn (G. Li), ljliu2@163.com (L. Liu), jhlin@pku.edu.cn (J. Lin).

https://doi.org/10.1016/j.ssc.2022.115051
Received 20 July 2022; Received in revised form 25 November 2022; Accepted 14 December 2022
Available online 21 December 2022

superconductors have grown to a unique family [29,30]. They all crystalize in perovskite structure with a typical ABO_3 formula. The cation at the B site is six coordinated by the anions at the O site to form BO_6 octahedra, which connect by corner-sharing of the anions at the O site to build a three-dimensional network [29]. This is helpful to build the three-dimensional superconductivity in these $BaBiO_3$ based superconductors. The cations at A site occupy the cavities surrounding by eight corner-sharing BO_6 octahedra. This structure is very flexible. Many different cations can appear at the A and B sites for the $BaBiO_3$ based superconductors, such as Na^+, K^+, Rb^+, Sr^{2+}, Ba^{2+}, Y^{3+}, La^{3+}, Ce^{4+}, Pr^{3+}(and/or Pr^{4+}), Nd^{3+}, Sm^{3+}, Eu^{3+}, Gd^{3+}, Tb^{3+}, Dy^{3+}, Ho^{3+}, Er^{3+}, Tm^{3+}, Yb^{3+}, Lu^{3+}, and Bi^{3+} are found in the A site [31–40], Na^+, Tl^{3+}, Bi^{3+}, Bi^{5+}, Pb^{2+}, Pb^{4+}, Mg^{2+}, Sb^{5+} and In^{3+} are found in the B site [41–46]. Different from Bi^{3+}, Bi^{5+}, Pb^{2+}, Pb^{4+} and In^{3+}, only $KBa_3(Bi_{0.89}Na_{0.11})_4O_{12}$ [41], $BaBi_{0.25}Tl_{0.25}Pb_{0.50}O_{3-\delta}$ [42], $Ba_{0.62}K_{0.38}Bi_{0.92}Mg_{0.08}O_3$ [44], are reported to be superconductor with Na^+, Tl^{3+}, and Mg^{2+} at the B site respectively. Therefore, it is very interesting to synthesize more $BaBiO_3$ based superconductors with Na^+, Tl^{3+}, Mg^{2+}, or other cation which has not been reported in the B site. Herein, the synthesis of solid solution $Ba(Bi_{0.25}Pb_{0.75})_{1-x}Mg_xO_{3-\delta}$ ($0 \le x \le 0.10$) through the solid-state method is reported. It is found that T_C^{zero} decreases very slowly from 11.2 K for $BaBi_{0.25}Pb_{0.75}O_{3-\delta}$ to 9.2 K for $Ba(Bi_{0.25}Pb_{0.75})_{0.90}Mg_{0.10}O_{3-\delta}$, which is higher than 7 K for $Ba_{0.62}K_{0.38}Bi_{0.92}Mg_{0.08}O_3$ [44]. This decrease is related to the departure from the optimal hole-doping state of $BaBi_{0.25}Pb_{0.75}O_{3-\delta}$ by Mg^{2+} doping and oxygen vacancies changing in the sample $Ba(Bi_{0.25}Pb_{0.75})_{1-x}Mg_xO_{3-\delta}$.

2. Experimental

The $Ba(Bi_{0.25}Pb_{0.75})_{1-x}Mg_xO_{3-\delta}$ (x = 0.00, 0.01, 0.02, 0.03, 0.04, 0.05, 0.06, 0.07, 0.08, 0.09, 0.10, 0.12, 0.14, 0.16, 0.18,and 0.20, denoted as Mg1, Mg2, …, and Mg16, respectively) samples have been synthesized from MgO (99.9%), $BaCO_3$ (99.9%), Bi_2O_3 (99.9%), as well as PbO (99.9%). The oven-dried raw materials were weighed according to the molar ratios of the nominal formula $Ba(Bi_{0.25}Pb_{0.75})_{1-x}Mg_xO_{3-\delta}$ and were ground using an agate mortar and a pestle for about 30 min, as well as calcined at 760 °C for 12 h. Then the calcined materials were ground again, pressed into pellets under 30 MPa, and re-calcined at 780 °C for 12 h. The materials were re-ground and re-pressed into cylindrical pellets to undertake five thermal treatments for 12 h at 820 °C (x = 0.00, Mg1), 840 °C (x = 0.01, Mg2), 860 °C (x = 0.02, Mg3), 880 °C (x = 0.03, Mg4), 900 °C (x = 0.04, Mg5), 920 °C (x = 0.05, Mg6; x = 0.06, Mg7), 940 °C (x = 0.07, Mg8; x = 0.08, Mg9), 960 °C (x = 0.09, Mg10; x = 0.10, Mg11; x = 0.12, Mg12; x = 0.14, Mg13), 980 °C (x = 0.16, Mg14; x = 0.18, Mg15; x = 0.20, Mg16) for the samples with the nominal formula $Ba(Bi_{0.25}Pb_{0.75})_{1-x}Mg_xO_{3-\delta}$ respectively. All the treatments are a furnace cooling in the air every time with intermediate grinding and then pressing into pellets under 30 MPa. The above suitable treatment temperature for each sample was obtained by the following processes: (a) The samples are treated at a temperature (such as 820 °C) for five 12 h treatments, then the X-ray diffraction data of these samples are obtained and analyzed; If the X-ray diffraction data of a selected sample is belonged to a single phase, further treatment is not needed for this sample, the corresponding temperature is the suitable treatment temperature for this sample; (b) the other samples should be treated at a temperature higher than before for about 20 °C for five 12 h treatments following with the check of the X-ray diffraction data; (c) If the X-ray diffraction data of a selected sample is belonged to a single phase or is almost the same as that obtained last time (this means the equilibrium state is obtained for this sample), further treatment is not needed for this sample, this temperature is the suitable treatment temperature for this sample; otherwise, the process (b) is continued. PANalytical X'Pert Powder diffractometer was used to collect Powder X-ray diffraction (PXRD) data between 5 and 120° (2θ) at steps of 0.0131° for 2 h. The diffractometer produced Cu Kα (λ_1 = 0.15405 nm and λ_2 = 0.15443 nm) radiation at 40 kV and 40 mA at room temperature. Neutron powder diffraction (NPD) data of the samples Mg1, Mg3, Mg5, Mg9, Mg12, Mg14, and Mg15 at room temperature were obtained using the instrument Echidna at the OPAL reactor (Lucas Heights, Australia) of the Australian Nuclear Science and Technology Organization (ANSTO) at λ = 1.62150 Å. GSAS program was used to analyze the x-ray and neutron diffraction data [47,48]. Selected area electron diffractions (SAED) were performed on JEM2100 (accelerating voltage: 200 kV). The valence state of elements in the samples was investigated via the X-ray photoelectron spectroscopy (XPS) patterns using a UK Kratos Axis Ultra spectrometer. The chamber pressure was not more than 5.0×10^{-9} Torr. The electron binding energies were calibrated with the C 1s peak at E_b = 284.8 eV as a reference. The magnetic property and resistivity of $Ba(Bi_{0.25}Pb_{0.75})_{1-x}Mg_xO_{3-\delta}$ was tested via a cryogenic Physical Property Measurement System (PPMS, supplied by East Changing, China) from 2 to 20 K.

3. Results and discussion

3.1. Solid solution and structure of $Ba(Bi_{0.25}Pb_{0.75})_{1-x}Mg_xO_{3-\delta}$

Powder X-ray diffraction patterns of the samples Mg1 to Mg16 are similar each other as shown in Fig. 1. This may suggest that the structure of the main phase in each sample is similar as that of Mg1 ($BaBi_{0.25}Pb_{0.75}O_{3-\delta}$), which has been confirmed to crystallize in a triclinic space group $P1$ previously [46]. SAED patterns of several samples have been checked, which can be well indexed by the triclinic space group $P1$ with similar lattice parameters of Mg1 ($a \approx 6.063$ Å, $b \approx 6.057$ Å, $c \approx 6.070$ Å, $\alpha \approx 60.23°$, $\beta \approx 59.87°$, and $\gamma \approx 60.04°$). Therefore, the structural parameters for Mg1 are used as the starting model to refine the X-ray and neutron diffraction patterns of the samples Mg2 to Mg16. More diffraction peaks other than those of Mg1 can be found in the diffraction patterns for Mg15, and Mg16 as shown in Fig. 2c, which belongs to $BaCO_3$ [49]. In addition, although diffraction peaks corresponding to MgO [50] are not easy to be found in the X-ray diffraction patterns of Mg15, they can be found in the neutron diffraction patterns of Mg15, which are shown in Fig. 2d. After careful checking, the diffraction peaks corresponding to $BaCO_3$ and MgO are also found in the

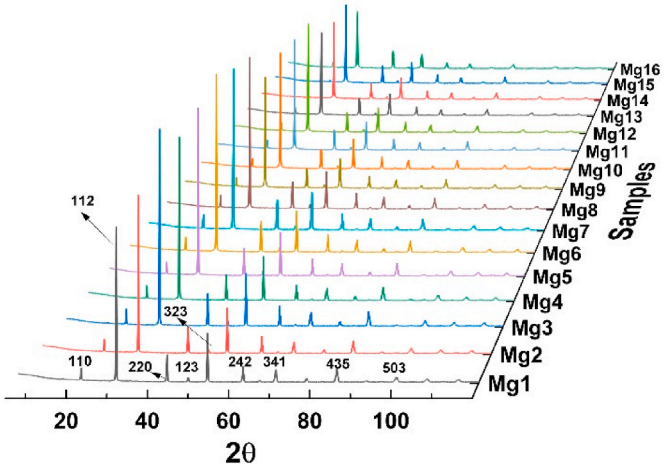

Fig. 1. X-ray diffraction data of the sample with the nominal formula $Ba(Bi_{0.25}Pb_{0.75})_{1-x}Mg_xO_{3-\delta}$. (x = 0.00 (Mg1), 0.01 (Mg2), 0.02 (Mg3), 0.03 (Mg4), 0.04 (Mg5), 0.05 (Mg6), 0.06 (Mg7), 0.07 (Mg8), 0.08 (Mg9), 0.09 (Mg10), 0.10 (Mg11), 0.12 (Mg12), 0.14 (Mg13), 0.16 (Mg14), 0.18 (Mg15), and 0.20 (Mg16)). The indexes shown near the X-ray diffraction data of Mg1 are based on triclinic cell $a \approx 6.064$, $b \approx 6.057$, $c \approx 6.065$ Å, $\alpha \approx 60.22°$, $\beta \approx 59.92°$, $\gamma \approx 60.04°$. Because $a \approx b \approx c$, $\alpha \approx \beta \approx \gamma$, the index abc (such as 123) includes bac (213), bca (231), acb (132), cab (312), cba (321), and so on. In addition, for the limit of space, several indexes are not shown. For example, there are also indexes (20 $\bar{2}$), (02 $\bar{2}$), (2 $\bar{2}$ 0) for the peaks around the index (242).

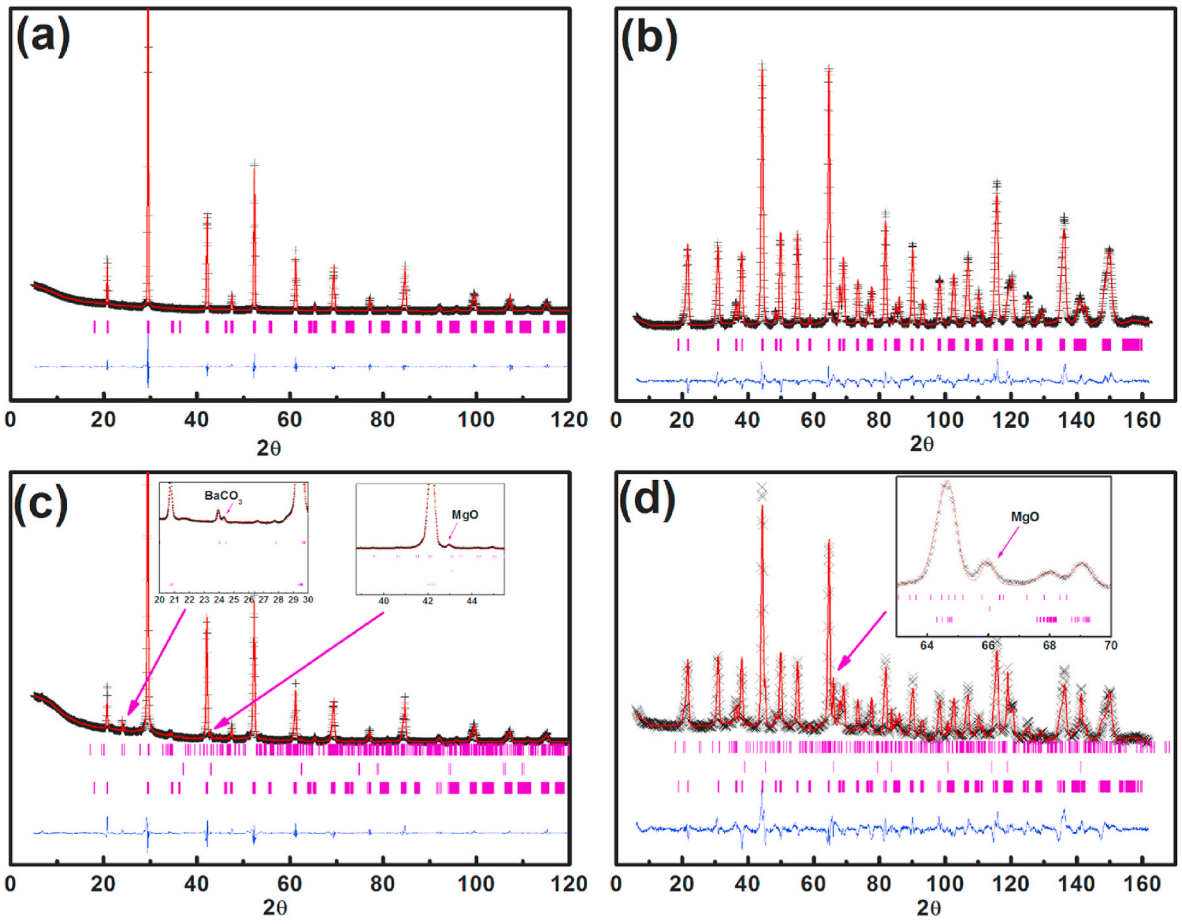

Fig. 2. Rietveld plot of the X-ray (a, Mg5; c, Mg15) and neutron diffraction data (b, Mg5; d, Mg15) of the selected samples at room temperature. The plus symbol represents the observed value, the solid line represents the calculated value, the marks below the diffraction patterns are the calculated reflection positions, and the difference curve is shown at the bottom in the figure.

X-ray diffraction data of Mg12, Mg13, Mg14, and the neutron diffraction data of Mg12 and Mg14. In this case, the X-ray and Neutron diffraction data of Mg12 to Mg16 are refined using three phases; the main phase with a structure similar to Mg1, $BaCO_3$ phase, and MgO phase. The refinements are acceptable with $R_{wp}^x < 0.07$ and $R_p^x < 0.05$ for X-ray diffraction data, $R_{wp}^n < 0.06$ and $R_p^n < 0.05$ for neutron diffraction data. The samples Mg1 to Mg11 are single-phase. The corresponding refinements are very nice as shown in Fig. 2 for Mg5 with $R_{wp}^x < 0.05$ and $R_p^x < 0.04$ for X-ray diffraction data, and $R_{wp}^n < 0.06$ and $R_p^n < 0.05$ for neutron diffraction data.

The unit cell volume of the $Ba(Bi_{0.25}Pb_{0.75})_{1-x}Mg_xO_{3-\delta}$ phase in the studied samples has been obtained with the help of the Rietveld refinement, which is shown in Fig. 3. The unit cell volume increases linearly with an enhancement of Mg in the samples with the nominal formula $Ba(Bi_{0.25}Pb_{0.75})_{1-x}Mg_xO_{3-\delta}$ when $x < 0.10$, which agrees well with Vegard's law [51,52]. When $x > 0.10$, the unit cell volume of the $Ba(Bi_{0.25}Pb_{0.75})_{1-x}Mg_xO_{3-\delta}$ phase reaches a constant. Therefore, the solid solution limit is about $x = 0.10(1)$. Impurities such as $BaCO_3$ and MgO are found in the samples with the nominal formula $Ba(Bi_{0.25}Pb_{0.75})_{1-x}Mg_xO_{3-\delta}$ when $x > 0.10$ as mentioned above.

The increase of the unit cell volume of $Ba(Bi_{0.25}Pb_{0.75})_{1-x}Mg_xO_{3-\delta}$ phase with an increase of Mg in the sample is surprising. As well known, the ionic radius of Mg^{2+} ($r_{Mg^{2+}} = 0.72$ Å (6-coordinated)) is smaller than that of Bi^{3+} ($r_{Bi^{3+}} = 1.03$ Å (6-coordinated)), Bi^{5+} ($r_{Bi^{5+}} = 0.76$ Å (6-coordinated)), Pb^{2+} ($r_{Pb^{2+}} = 1.19$ Å (6-coordinated)), and Pb^{4+} ($r_{Pb^{4+}} = 0.775$ Å (6-coordinated)). It is reasonable to expect that the unit cell volume of $Ba(Bi_{0.25}Pb_{0.75})_{1-x}Mg_xO_{3-\delta}$ phase should decrease with an increase of Mg in the sample as reported for the solid solution $BaBi_{1-x}Ta_xO_3$ [53]. Similar phenomenon has been reported for the solid solutions $Ba_{1-x}Pr_x(Bi_{0.20}Pb_{0.80})O_{3-\delta}$ ($0 \le x \le 0.17$) and $Ba_{1-x}Ce_x(Bi_{0.20}Pb_{0.80})O_{3-\delta}$ ($0 \le x \le 0.16$) [30]. Although the radius of Ce^{4+} ($r_{Ce^{4+}} = 0.97$ Å) (eight coordinated)), Pr^{4+} ($r_{Pr^{4+}} = 0.96$ Å) (eight coordinated)), or Pr^{3+} ($r_{Pr^{3+}} = 1.126$ Å) (eight coordinated)) is smaller than that of Ba^{2+} ($r_{Ba^{2+}} = 1.42$ Å) (eight coordinated)), the unit cell volume of solid solutions $Ba_{1-x}Pr_x(Bi_{0.20}Pb_{0.80})O_{3-\delta}$ ($0 \le x \le 0.17$) and $Ba_{1-x}Ce_x(Bi_{0.20}Pb_{0.80})O_{3-\delta}$

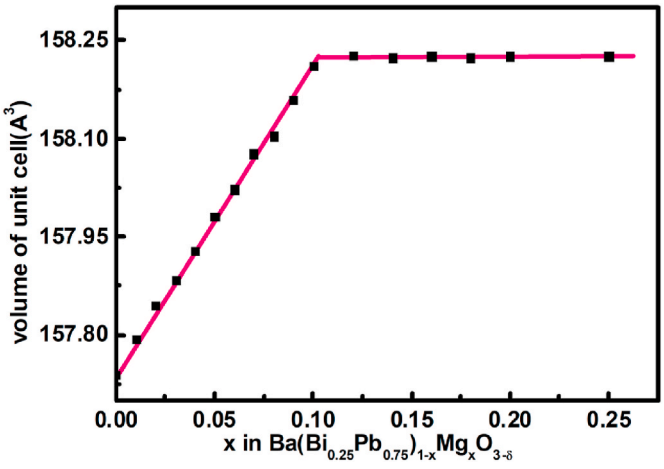

Fig. 3. Composition dependent unit cell volume of $Ba(Bi_{0.25}Pb_{0.75})_{1-x}Mg_xO_{3-\delta}$.

($0 \leq x \leq 0.16$) increases with an increase of Ce or Pr in the samples. This has been attributed to that in order to balance the charge of the sample, the increase of Ce^{4+}, Pr^{4+}, or Pr^{3+} will increase Bi^{3+}(and/or Pb^{2+}) and decrease Bi^{5+}(and/or Pb^{4+}) in the sample. Then the average radius of the atoms at the B site will increase, which may increase the unit cell volume. More details are discussed in the previous work on $Ba_{1-x}Ln_x(-Bi_{0.20}Pb_{0.80})O_{3-\delta}$ (Ln = La, Ce, Pr, Nd, Sm, Eu, Gd, Tb, Dy, Ho, Er, Tm, Yb, Lu) [30]. If one considers the above charge balance effect, the increase of Mg in the samples $Ba(Bi_{0.25}Pb_{0.75})_{1-x}Mg_xO_{3-\delta}$ should induce more Bi^{5+}(and/or Pb^{4+}) and less Bi^{3+}(and/or Pb^{2+}) under an assumption that δ is almost the same for all the samples, which will cause a decrease of the unit cell volume because the radius of Bi^{5+}(Pb^{4+}) is smaller than that of Bi^{3+}(Pb^{2+}). However, this is not agreed with the present experimental data. Then, one may argue that oxygen vacancies are involved in the balance of the charge. Maybe some Bi^{5+}(Pb^{4+}) is converted to Bi^{3+}(Pb^{2+}) due to an increase of oxygen vacancies to increase the unit cell volume. In order to validate this assumption, in the next sections, the amount of oxygen vacancies in the samples was assessed by XPS and iodometric titration.

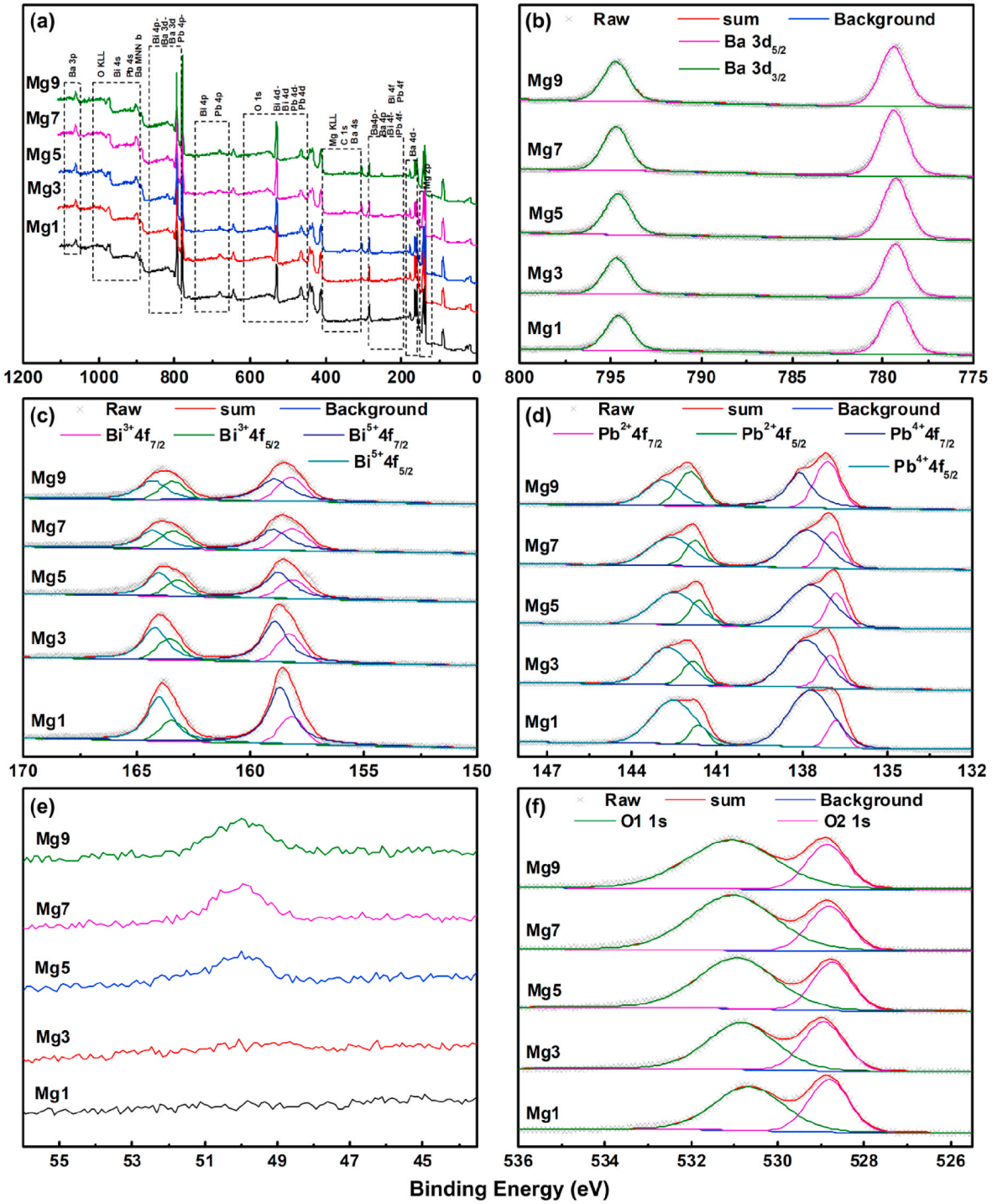

Fig. 4. Binding energies of the survey (a), Ba (b), Bi (c), Pb (d), Mg (e), and O (f) of $Ba(Bi_{0.25}Pb_{0.75})_{1-x}Mg_xO_{3-\delta}$ ($x = 0.00$, Mg1;$x = 0.02$, Mg3; $x = 0.04$, Mg5; $x = 0.06$, Mg7; $x = 0.08$, Mg9).

3.2. Valence of Ba, Bi, Pb, Mg, and O in $Ba(Bi_{0.25}Pb_{0.75})_{1-x}Mg_xO_{3-\delta}$

X-ray photoelectron spectroscopy (XPS) data of selected samples Mg1, Mg3, Mg5, Mg7, and Mg9 belonging to the solid solution Ba$(Bi_{0.25}Pb_{0.75})_{1-x}Mg_xO_{3-\delta}$ ($0 \leq x \leq 0.10$) are shown in Fig. 4. The survey spectrum (Fig. 4a) indicates that Ba, Bi, Pb, Mg, and O elements are present in the sample (where the C element is produced by the XPS instrument itself). The high-resolution Ba 3 d spectrum (Fig. 4b) shows two symmetric peaks at 779.27 and 794.56 eV corresponding to $3d_{5/2}$ and $3d_{3/2}$ of Ba^{2+} ions [54]. No obvious changes occur in the doped samples. This suggests that the valence state of Ba remains unchanged. The XPS spectra of Bi $4f_{7/2}$, Bi $4f_{5/2}$, Pb $4f_{7/2}$, and Pb $4f_{5/2}$ given in Fig. 4c and d are doublets. The peaks corresponding to Bi $4f_{7/2}$, Bi $4f_{5/2}$, Pb $4f_{7/2}$, and Pb $4f_{5/2}$ can be fitted for two peaks, $4f_{7/2}$ of Bi^{3+} (158.2 eV) and Bi^{5+} (158.9 eV), $4f_{5/2}$ of Bi^{3+} (163.5 eV) and Bi^{5+} (164.2 eV), $4f_{7/2}$ of Pb^{2+} (136.9 eV) and Pb^{4+} (137.7 eV), and $4f_{5/2}$ of Pb^{2+} (141.7 eV) and Pb^{4+} (142.5 eV) [46,55,56]. Table 1 shows the ratios of Bi^{3+}:Bi^{5+} and Pb^{2+}:Pb^{4+} in each sample analyzed by XPS. With an increase of Mg in the sample, the ratios of Bi^{3+}: Bi^{5+} and Pb^{2+}: Pb^{4+} increase, which suggests that the relative amount of Bi^{3+} (Pb^{2+}) increases. This may be the reason why the unit cell volume increases with an increase of Mg in the samples.

XPS of Mg 2p has no obvious signal for Mg1 as shown in Fig. 4e. With an increase of Mg in the sample, the corresponding peaks for Mg^{2+} occur around 50 eV and then enhance. The O 1s spectrum has two peaks assigned at O1 1s (528.81 eV) and O2 1s (530.65 eV) corresponds to O^{2-} ions without the oxygen vacancy in the near neighbor and O^{2-} ions with the oxygen vacancy in the near neighbor, respectively (Fig. 4f) [57,58]. The intensity of O2 1s peak ($I_{O2^{1s}}$) gradually enhances with increase of Mg, which suggests that the oxygen vacancy gradually increases. The ratio $I_{O2^{1s}} : I_{O1^{1s}}$ for each sample is listed in Table 2.

3.3. Oxygen vacancy in $Ba(Bi_{0.25}Pb_{0.75})_{1-x}Mg_xO_{3-\delta}$

XPS analysis qualitatively determines the presence of oxygen vacancies in the samples. To quantitively estimate the oxygen vacancies, an iodometric titration is performed for representative samples. The corresponding data is shown in Fig. 5a. The oxygen vacancies increase with an increase of Mg in the solid solution $Ba(Bi_{0.25}Pb_{0.75})_{1-x}Mg_xO_{3-\delta}$. Given that the samples are neutral, it is reasonable to deduce that the number of the electron per 6 S orbital from the obtained value of oxygen vacancy decreases with increasing Mg content in the samples, which in turn means an increase in the content of holes in the samples. Comparing the data shown in Figs. 4f and 5a, it is interesting that even for the sample Mg1 where the content of oxygen vacancy is only about 1% the intensity of XPS peak O2 1s related to the oxygen with "direct" interaction to oxygen vacancy is stronger than that of O1 1s related to the oxygen without "direct" interaction to oxygen vacancy. However, when the content of oxygen vacancy reaches about 2% for the sample Mg5 the corresponding intensity of XPS peak O2 1s does not double.

This may mean that the relationship between the content of oxygen vacancy and the intensity of XPS peak O2 1s is not linear. A quadratic function model is suggested as below:

$$R = A\,\delta + B\,\delta^2 \quad (1)$$

Table 2
Binding energies (eV) of O 1s and the ratio of $I_{O2^{1s}} : I_{O1^{1s}}$ for $Ba(Bi_{0.25}Pb_{0.75})_{1-x}Mg_xO_{3-\delta}$

	O1 1s	O2 1s	$I_{O2^{1s}} : I_{O1^{1s}}$
Mg1	528.81	530.65	0.633:0.367
Mg3	528.93	530.81	0.647:0.353
Mg5	528.73	530.92	0.719:0.281
Mg7	528.80	531.00	0.785:0.215
Mg9	528.86	531.03	0.760:0.240

Here, R is the ratio of $I_{O2^{1s}} : I_{O1^{1s}}$, δ the content of oxygen vacancy in the sample $Ba(Bi_{0.25}Pb_{0.75})_{1-x}Mg_xO_{3-\delta}$. The fitting result is shown in Fig. 5b. Two data from $Ba(Bi_{0.25}Pb_{0.75})_{1-x}In_xO_{3-\delta}$ [46] are also used, which are marked by a triangle in Fig. 5b. The origin marked by the square is suggested under the consideration that if there is no oxygen vacancy the intensity of XPS peak O2 1s should be zero. The fitting of the present data by the above quadratic function model seems acceptable. More precise data should be obtained to help the establishment of the relationship between the intensity of XPS peak O2 1s and the content of oxygen vacancy in the sample.

3.4. Superconductivity of $Ba(Bi_{0.25}Pb_{0.75})_{1-x}Mg_xO_{3-\delta}$

Typical magnetic susceptibilities for the studied samples have been shown as the inset of Fig. 6a. When the temperature decreases, the magnetic susceptibilities start to drop to more minus value around ~11 K–~12 K for all samples, which is noted as T_C^{mag}. For the pure single-phase sample, such as Mg1, Mg2, Mg5, or Mg7, the drop is obvious. When the sample contains some impurity such as $BaCO_3$ and MgO as mentioned above, the drop is gentle as shown in Fig. 6a for Mg11 and Mg16. This is due to the decrease of the component of superconductor phase in the samples. The composition-dependent shielding volume fraction of the studied samples at 8 K is shown in Fig. 6a. With an increase of Mg in the nominal formula $Ba(Bi_{0.25}Pb_{0.75})_{1-x}Mg_xO_{3-\delta}$, the shielding volume fraction decreases, which means that the superconductive component decreases.

Temperature dependent resistance of the samples Mg1 to Mg16 was measured between 2 and 20 K. Typical data were shown in Fig. 6b and c for the samples Mg2, and Mg13. The electrical resistance of all samples increases when the temperature decreases to a certain temperature, after that the electrical resistance begins to decrease sharply. This temperature is noted as T_C^{onset}, which is very close to T_C^{mag} of the corresponding sample. With the further decrease of temperature, zero resistance can be reached for all samples below a certain temperature (noted as T_C^{zero}). The composition-dependent T_C^{zero} for $Ba(Bi_{0.25}Pb_{0.75})_{1-x}Mg_xO_{3-\delta}$ are displayed in Fig. 6d. T_C^{zero} tends to decrease with an increase of Mg for Ba$(Bi_{0.25}Pb_{0.75})_{1-x}Mg_xO_{3-\delta}$ ($0 \leq x \leq 0.10$) as indicated by the solid line shown in Fig. 6d. This may be related to the decrease of the electrons in the 6 S orbital as shown in Fig. 5a, which makes the sample deviate from the optimal hole-doping state of $BaBi_{0.25}Pb_{0.75}O_{3-\delta}$. This result is similar to that reported for $Ba(Bi_{0.25}Pb_{0.75})_{1-x}In_xO_{3-\delta}$ [45]. One may find that the values T_C^{zero} for $Ba(Bi_{0.25}Pb_{0.75})_{1-x}Mg_xO_{3-\delta}$ and $Ba(Bi_{0.25}Pb_{0.75})_{1-x}In_xO_{3-\delta}$ are almost the same if the number of the electron per 6 S orbital in both samples are the same. The zero resistivity can also be measured for the sample with some impurities. With an increase of impurities, the

Table 1
Binding energies (eV) of Bi $4f_{7/2}$, Bi $4f_{5/2}$, Pb $4f_{7/2}$, Pb $4f_{5/2}$, the ratio of Bi^{3+}:Bi^{5+} and Pb^{2+}:Pb^{4} for $Ba(Bi_{0.25}Pb_{0.75})_{1-x}Mg_xO_{3-\delta}$

	$4f_{7/2}$		$4f_{5/2}$		Bi^{3+}:Bi^{5+}	$4f_{7/2}$		$4f_{5/2}$		Pb^{2+}:Pb^{4+}
	Bi^{3+}	Bi^{5+}	Bi^{3+}	Bi^{5+}		Pb^{2+}	Pb^{4+}	Pb^{2+}	Pb^{4+}	
Mg1	158.17	158.69	163.44	164.01	0.25:0.75	136.80	137.70	141.64	142.54	0.14:0.86
Mg3	158.27	158.93	163.56	164.21	0.32:0.68	136.98	137.79	141.82	142.63	0.15:0.85
Mg5	158.13	158.77	163.19	164.01	0.35:0.65	136.80	137.59	141.63	142.42	0.18:0.82
Mg7	158.16	158.97	163.37	164.30	0.40:0.60	136.90	137.65	141.77	142.50	0.20:0.80
Mg9	158.20	158.95	163.41	164.30	0.42:0.58	136.92	137.77	141.80	142.62	0.22:0.78

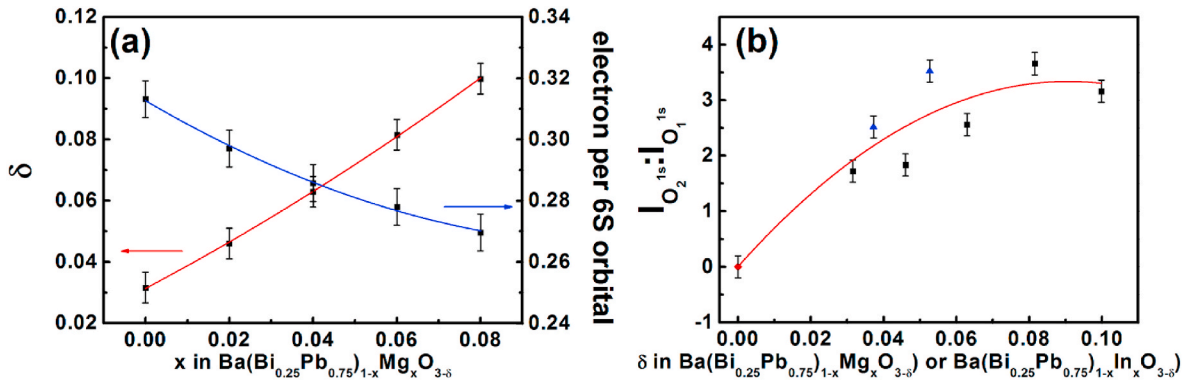

Fig. 5. The composition-dependent oxygen vacancy δ and electron per 6 S orbital of $Ba(Bi_{0.25}Pb_{0.75})_{1-x}Mg_xO_{3-\delta}$ (a), the relationship between the ratio of $I_{O2^{1s}} : I_{O1^{1s}}$ and oxygen vacancy δ for $Ba(Bi_{0.25}Pb_{0.75})_{1-x}Mg_xO_{3-\delta}$ (b). The data shown by squares and circles in Fig. 5b are from $Ba(Bi_{0.25}Pb_{0.75})_{1-x}In_xO_{3-\delta}$ [45] and $Ba(Bi_{0.25}Pb_{0.75})_{1-x}Mg_xO_{3-\delta}$, respectively.

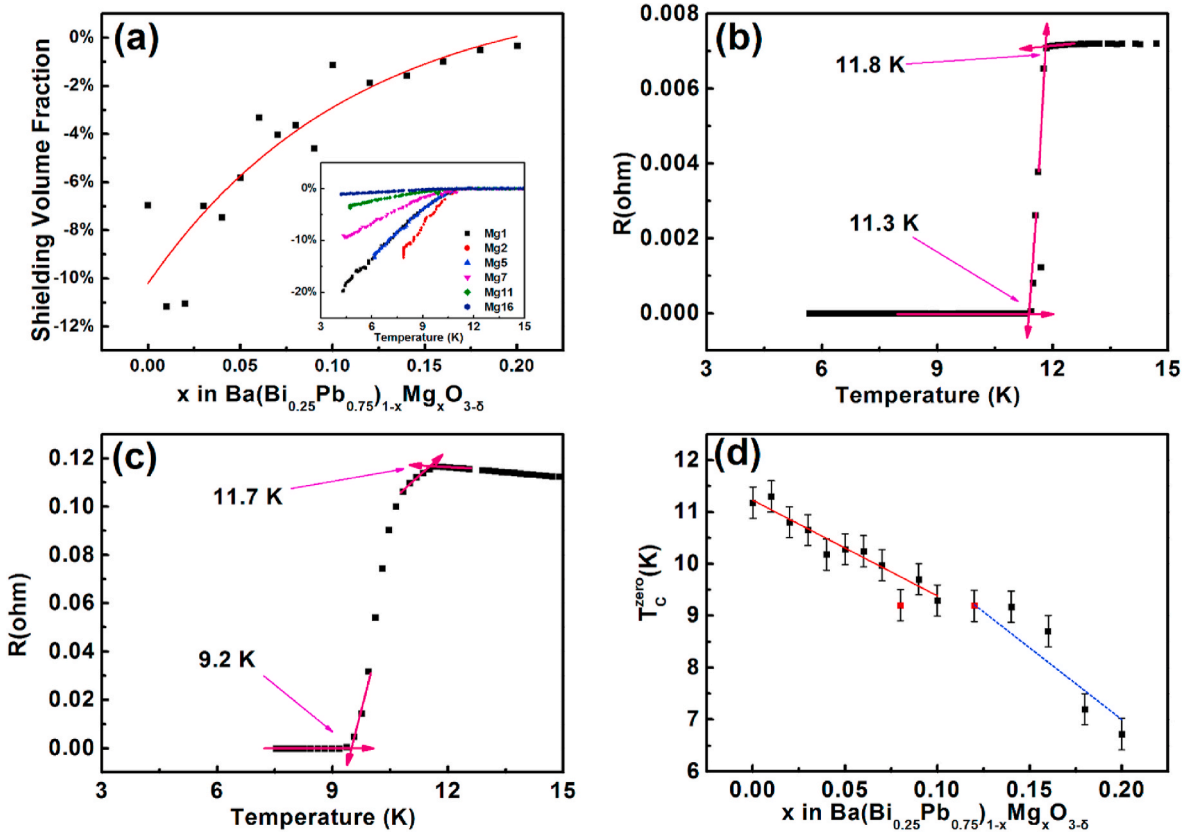

Fig. 6. Composition-dependent shielding volume fraction for $Ba(Bi_{0.25}Pb_{0.75})_{1-x}Mg_xO_{3-\delta}$ **(a)**, temperature-dependent resistance of Mg2 **(b)** and Mg13 **(c)**, and composition-dependent T_C^{zero} for $Ba(Bi_{0.25}Pb_{0.75})_{1-x}Mg_xO_{3-\delta}$ **(d)**. Inset gives dc magnetic susceptibility curves of Mg1, Mg2, Mg5, Mg7, Mg11, and Mg16 under a measured magnetic field of 500 Oe.

measured T_C^{zero} tends to decrease as shown by the dot line in Fig. 6d, which may mean that the existence of impurities may affect the number of the electron per 6 S orbital in the sample to change the T_C^{zero} of the corresponding sample.

It is interesting that although the shielding volume fraction of the studied sample at 8 K is lower than 20%, the "zero" resistance can be measured above 8 K for most of the studied samples. The low shielding volume fraction reported here seems comparable to that reported for $Ba_{0.60}K_{0.40}BiO_{3-\delta}$ [28], but is significantly lower than that reported for $(Ba_{0.62}K_{0.38})(Bi_{0.92}Mg_{0.08})O_3$ [44]. It is also interesting that a very narrow gap (about 0.5 K) between T_C^{onset} and T_C^{zero} is observed for some of our bulk samples such as Mg2 shown in Fig. 6b, which may cause a wrong impression that T_C^{zero} of Mg2 may be better than its T_C^{mag} if one compares the data shown in Fig. 6b and the inset of Fig. 6a. Of course, the basic reason for this is the thermometers to monitor the temperature of the sample for magnetic and resistance measurement are different in our liquid helium free cryogenic Physical Property Measurement (PPMS, supplied by East Changing, China), which are denoted as T^{mag} and T^{res} respectively. For resistance measurement, the thermometer is along with the sample. And for magnetic measurement, the thermometer is a little far from the sample. In our system, the difference between T^{mag} could be 0.5 K lower than T^{res} at the steady measurement condition below 30 K. Therefore, there is a chance to observe that T_C^{zero} of a certain sample is very closed to its T_C^{mag}.

As shown in Fig. 6d, T_C^{zero} of all $Ba(Bi_{0.25}Pb_{0.75})_{1-x}Mg_xO_{3-\delta}$ ($0 \le x \le 0.10$) is above 9.2 K, which is little higher than 7 K reported for $(Ba_{0.62}K_{0.38})(Bi_{0.92}Mg_{0.08})O_3$ [44]. The difference among them may be related to the different hole-doping states discussed below. $(Ba_{0.62}K_{0.38})(Bi_{0.92}Mg_{0.08})O_3$ is related to $(Ba_{1-x}K_x)BiO_3$ with a maximum T_C of about 34 K [59]. As reported by S. Y. Pei et al. [60], T_C of $(Ba_{1-x}K_x)BiO_3$ changes with the change of K in the samples with a maximum of T_C at about $x = 0.40$, which is explained as that optimal-doped state is realized around $x = 0.40$ [61]. When more or less Ba^{2+} cations are replaced by K^+, more or fewer holes appear which causes the decrease of T_C [59]. Put simply, when x Ba^{2+} is replaced by x K^+ in $BaBiO_3$ to form $Ba_{1-x}K_xBiO_3$, there will be x hole in the compound $Ba_{1-x}K_xBiO_3$. When $y/2Bi^{5+} + y/2Bi^{3+}$ are replaced by y Mg^{2+} in $BaBiO_3$ (It is suggested that $BaBiO_3$ should be noted as $Ba_2Bi^{III}Bi^{V}O_6$ [29]) to form $BaBi_{1-y}Mg_yO_3$, there will be $2y$ hole in the compound $BaBi_{1-y}Mg_yO_3$. As a result, there are about 0.4 hole per $Ba_{0.60}K_{0.40}BiO_3$, and 0.56 ($0.38 + 2 \times 0.08$) hole per $(Ba_{0.62}K_{0.38})(Bi_{0.92}Mg_{0.08})O_3$. Therefore, it is reasonable to find the T_C of $(Ba_{0.62}K_{0.38})(Bi_{0.92}Mg_{0.08})O_3$ is just about 7 K following the trend shown in (Fig. 2) of the reported work by S. Y. Pei et al. [60].

The superconductor $Ba(Bi_{0.25}Pb_{0.75})_{1-x}Mg_xO_{3-\delta}$ ($0 \le x \le 0.10$) reported in our manuscript is related to hole-doped superconductors $BaPb_{1-x}Bi_xO_{3-\delta}$ with an optimal hole-doping state around $x = 0.22$ reported by Z. F. Wu et al. [62]. When $x < 0.22$, more Pb are doped in the sample $BaPb_{1-x}Bi_xO_{3-\delta}$, which means that there are more holes in the sample. T_C of the corresponding $BaPb_{1-x}Bi_xO_{3-\delta}$ will decreases as indicated by Z. F. Wu et al. [61]. For simplicity, $BaPb_{0.75}Bi_{0.25}O_3$ is suggested as the optimal hole-doping sample. When x Bi is replaced by x Pb, x hole will be added in the sample $BaPb_{0.75+x}Bi_{0.25-x}O_3$. At the same time, when x $Bi_{0.25}Pb_{0.75}$ is replaced by x Mg, $2x$ hole will be added in the sample $Ba(Bi_{0.25}Pb_{0.75})_{1-x}Mg_xO_3$. For the sample $Ba(Bi_{0.25}Pb_{0.75})_{0.90}Mg_{0.10}O_3$, there are more 0.20 holes per $Ba(Bi_{0.25}Pb_{0.75})_{0.90}Mg_{0.10}O_3$ than that for the optimal hole-doping sample $BaPb_{0.75}Bi_{0.25}O_3$. Then following the trend shown in (Fig. 4) of the reported work by Z. F. Wu et al. [62], T_C for $Ba(Bi_{0.25}Pb_{0.75})_{0.90}Mg_{0.10}O_3$ should be below 5 K. However, as shown in Fig. 5, oxygen vacancies increase with an increase of Mg in our samples $Ba(Bi_{0.25}Pb_{0.75})_{1-x}Mg_xO_{3-\delta}$, which decreases holes in the samples. As a result, T_C of about 9.2 K is obtained for our sample $Ba(Bi_{0.25}Pb_{0.75})_{0.90}Mg_{0.10}O_{3-\delta}$.

4. Conclusions

The solid solution $Ba(Bi_{0.25}Pb_{0.75})_{1-x}Mg_xO_{3-\delta}$ ($0 \le x \le 0.10$) has been synthesized by a conventional solid-state method. The volume of the unit cell obtained by Rietveld refinement increases with an increase of Mg in the solid solution. XPS data indicate that amount of Bi^{3+} (Pb^{2+}) increases with an increase of Mg, which may be the reason why the unit cell volume increases. T_C^{zero} of $Ba(Bi_{0.25}Pb_{0.75})_{1-x}Mg_xO_{3-\delta}$ ($0 \le x \le 0.10$) gradually decreases with an increase of Mg in the sample. This is related to the decrease of the number of the electron per 6 S orbital caused by Mg^{2+} doping and oxygen vacancies that appeared in the sample $Ba(Bi_{0.25}Pb_{0.75})_{1-x}Mg_xO_{3-\delta}$. At this case, $Ba(Bi_{0.25}Pb_{0.75})_{1-x}Mg_xO_{3-\delta}$ ($0 \le x \le 0.10$) is hole over-doped superconductor similar to $Ba(Bi_{0.25}Pb_{0.75})_{1-x}In_xO_{3-\delta}$ [46].

Credit author statement

Xiande Zheng synthesized the samples, collected and analyzed the X-ray diffraction data of the samples, prepared the manuscript. Muhammad Asim Farid analyzed the X-ray diffraction data of the samples and prepared the manuscript. Xiaoge Wang obtained and analyzed the selected area electron diffraction data of the samples. Yan Wang and Jinling Geng evaluated the quantity of the oxygen vacancies in the samples by an iodometric titration. Fuhui Liao collected and analyzed the X-ray diffraction data of the samples. Junliang Sun help to analyze the structure of the studied samples. Guobao Li designed the study program, measured the resistivity of the samples, and prepared the manuscript. Laijun Liu analyzed the XPS data of the samples and prepared the manuscript. Jianhua Lin designed the study program and prepared the manuscript.

Declaration of competing interest

The authors declare that they have no known competing financial interests or personal relationships that could have appeared to influence the work reported in this paper.

Data availability

Data will be made available on request.

Acknowledgments

This work is supported by the National Natural Science Foundation of China (Grant 21771007). The measurements of selected area electron diffractions (SAED), X-ray photoelectron spectroscopy (XPS) patterns, and Powder X-ray diffraction (PXRD) data were performed at the Analytical Instrumentation Center of Peking University. We acknowledge the assistance and support from Dr. Jing Ju, Jinglin Xie, and Jie Su respectively. We thank Dr. M. Avdeev for his assistance in collecting the neutron powder diffraction data at the OPAL facility.

Appendix A. Supplementary data

Supplementary data to this article can be found online at https://doi.org/10.1016/j.ssc.2022.115051.

Supporting Information

The SAED patterns, the refinement details of the X-ray and neutron diffraction data.

References

[1] E. Moser, E. Laistler, F. Schmitt, G. Kontaxis, Ultra-high field NMR and MRI–the role of magnet Technology to increase sensitivity and specificity, Front. Physiol. 5 (2017) 33.
[2] Z. Bunzarov, V. Dodokhov, A. Efremov, V. Golovatyuk, V. Ionaites, V. Kekelidze, O. Kovalchuk, E. Koshurnikov, Y. Lobanov, A. Makarov, V. Ochrimenko, A. Vodopyanova, Superconducting solenoid magnet for the Multi-Purpose Detector at the NICA facility, J. Instrum. 9 (2014), C09035.
[3] X.C. Xu, A review and prospects for Nb_3Sn superconductor development, Supercond. Sci. Technol. 30 (2017), 093001.
[4] Z.H. Mao, H. Jin, J.G. Qin, F. Liu, C. Dai, Q.B. Hao, C.S. Li, Axial tensile stress-strain characterization of Bi-2212 round wire with different heat treatments, IEEE Trans. Appl. Supercond. 27 (2017), 6400405.
[5] L. Ying, J. Sheng, B. Lin, L. Yao, J. Zhang, Z. Jin, Y. Li, Z. Hong, AC loss and contact resistance of resistive type fault current limiter using YBCO coated conductors, IEEE Trans. Appl. Supercond. 22 (2012), 5602204.
[6] A.P. Malozemoff, Progress in American superconductor's HTS wire and optimization for fault current limiting systems, Phys. C (Amsterdam, Neth.): Supercond. Appl. 530 (2016) 65–67.
[7] D. Larbalestier, A. Gurevich, D.M. Feldmann, A. Polyanskii, High-T-c superconducting materials for electric power applications, Nature 414 (2001) 368–377.
[8] G. Snitchler, B. Gamble, S.S. Kalsi, The performance of a 5 MW high temperature superconductor ship propulsion motor, IEEE Trans. Appl. Supercond. 15 (2005) 2206–2209.
[9] J.R. Hull, Superconducting bearings, Supercond. Sci. Technol. 13 (2000) R1–R15.
[10] M. Noe, M. Steurer, High-temperature superconductor fault current limiters: concepts, applications, and development status, Supercond. Sci. Technol. 20 (2007) R15–R29.
[11] L.W. Li, K. Nishimura, Giant reversible magnetocaloric effect in antiferromagnetic superconductor $Dy_{0.9}Tm_{0.1}Ni_2B_2C$ compound, Appl. Phys. Lett. 95 (2009), 132505.
[12] E. Snider, N. Dasenbrock-Gammon, R. McBride, M. Debessai, H. Vindana, K. Vencatasamy, K.V. Lawler, A. Salamat, R.P. Dias, Room-temperature superconductivity in a carbonaceous sulfur hydride, Nature 586 (2020) 373–377.

[13] Y. Cao, V. Fatemi, S. Fang, K. Watanabe, T. Taniguchi, E. Kaxiras, P. Jarillo-Herrero, Unconventional superconductivity in magic-angle graphene superlattices, Nature 556 (2018) 43–50.

[14] S. Ran, C. Eckberg, Q.P. Ding, Y. Furukawa, T. Metz, S.R. Saha, I.L. Liu, M. Zic, H. Kim, J. Paglione, N.P. Butch, Nearly ferromagnetic spin-triplet superconductivity, Science 365 (2019) 684–687.

[15] D. Li, K. Lee, B.Y. Wang, M. Osada, S. Crossley, H.R. Lee, Y. Cui, Y. Hikita, H. Y. Hwang, Superconductivity in an infinite-layer nickelate, Nature 572 (2019) 624–627.

[16] X.H. Chen, T. Wu, G. Wu, R.H. Liu, H. Chen, D.F. Fang, Superconductivity at 43 K in $SmFeAsO_{1-x}F_x$, Nature 453 (2008) 762, 762.

[17] C.W. Chu, L.Z. Deng, B. Lv, Hole-doped cuprate high temperature superconductors, Phys. C (Amsterdam, Neth.): Supercond. Appl. 514 (2015) 290–313.

[18] M. Rotta, M. Motta, A.L. Pessoa, C.L. Carvalho, C.V. Deimling, P.N. Lisboa-Filho, W.A. Ortiz, R. Zadorosny, One-pot-like facile synthesis of $YBa_2Cu_3O_{7-\delta}$ superconducting ceramic: using PVP to obtain a precursor solution in two steps, Mater. Chem. Phys. 243 (2020), 122607.

[19] Q. Ma, J. Peng, Z. Ma, F. Cheng, F. Lan, C. Li, Z. Yang, C. Liu, Y. Liu, Improved grain connectivity and critical current density in ex-situ MgB_2 superconductors prepared by two-step sintering, Mater. Chem. Phys. 204 (2018) 62–66.

[20] W.J. Zhang, L. Zheng, X.F. Zou, Q. Wang, X. Yu, Z. Yu, H. Zhang, Y. Zhao, Y. Zhang, A novel synthesis method for MgB_2 superconducting wires with kilometer-grade length, Ceram. Int. 45 (2019) 6413–6417.

[21] Y. Kamihara, T. Watanabe, M. Hirano, H. Hosono, Iron-based layered superconductor $La[O_{1-x}F_x]FeAs$ ($x = 0.05-0.12$) with Tc = 26 K, J. Am. Chem. Soc. 130 (2008) 3296–3297.

[22] C.C. Chang, T.K. Chen, W.C. Lee, P.H. Lin, M.J. Wang, Y.C. Wen, P.M. Wu, M. K. Wu, Superconductivity in Fe-chalcogenides, Phys. C (Amsterdam, Neth.): Supercond. Appl. 514 (2015) 423–434.

[23] H.Q. Yuan, J. Singleton, F.F. Balakirev, S.A. Baily, G.F. Chen, J.L. Luo, N.L. Wang, Nearly isotropic superconductivity in $(Ba,K)Fe_2As_2$, Nature 457 (2009) 565–568.

[24] G.W. Webb, F. Marsiglio, J.E. Hirsch, Superconductivity in the elements, alloys and simple compounds, Phys. C (Amsterdam, Neth.): Supercond. Appl. 514 (2015) 17–27.

[25] A.P. Drozdov, M.I. Eremets, I.A. Troyan, V. Ksenofontov, S.I. Shylin, Conventional superconductivity at 203 kelvin at high pressures in the sulfur hydride system, Nature 525 (2015) 73–76.

[26] F. Peng, Y. Sun, C.J. Pickard, R.J. Needs, Q. Wu, Y. Ma, Hydrogen clathrate structures in rare earth hydrides at high pressures: possible route to room-temperature superconductivity, Phys. Rev. Lett. 119 (2017), 107001.

[27] A.W. Sleight, J.L. Gillson, P.E. Bierstedt, High-temperature superconductivity in $BaPb_{1-x}Bi_xO_3$ system, Solid State Commun. 17 (1975) 27–28.

[28] R.J. Cava, B. Batlogg, J.J. Krajewski, R. Farrow, L.W. Rupp, A.E. White, K. Short, W.F. Peck, T. Kometani, Superconductivity near 30 K without copper – the $Ba_{0.6}K_{0.4}BiO_3$ perovskite, Nature 332 (1988) 814–816.

[29] A.W. Sleight, Bismuthates: $BaBiO_3$ and related superconducting phases, Phys. C (Amsterdam, Neth.): Supercond. Appl. 514 (2015) 152–165.

[30] M. Zhang, M.A. Farid, Y. Wang, J.L. Xie, J.L. Geng, H. Zhang, J.L. Sun, G.B. Li, F. H. Liao, J.H. Lin, Superconductivity in perovskite Ba1−xLnx(Bi0.20Pb0.80)O3−δ (Ln=La, Ce, Pr, Nd, Sm, Eu, Gd, Tb, Dy, Ho, Er, Tm, Yb, Lu),, Inorg. Chem. 57 (2018) 1269–1276.

[31] M. Braden, W. Reichardt, E. Elkaim, J.P. Lauriat, S. Shiryaev, S.N. Barilo, Structural distortion in superconducting $Ba_{1-x}K_xBiO_3$, Phys. Rev. B Condens. Matter 62 (2000) 6708–6715.

[32] M.H. Rubel, A. Miura, T. Takei, N. Kumada, M. Mozahar Ali, M. Nagao, S. Watauchi, I. Tanaka, K. Oka, M. Azuma, E. Magome, C. Moriyoshi, Y. Kuroiwa, A.K.M. Azharul Islam, Superconducting double perovskite Bismuth oxide prepared by a low-temperature hydrothermal reaction, Angew. Chem., Int. Ed. 53 (2014) 3599–3603.

[33] H. Zhang, X.H. Lin, Y.T. Zheng, S.E. Li, G.B. Li, F.H. Liao, J.H. Lin, Synthesis, structure, and properties of the superconductor $Ba_{1-x}K_zBi_{1-y}Pb_yO_3$, J. Supercond. Nov. Magnetism 28 (2015) 459–467.

[34] M.A. Farid, F.Y. Zhang, M. Zhang, H.X. Zhang, A. Firdous, G.B. Li, F.H. Liao, J. H. Lin, Superconductivity for potassium doped $BaPb_{0.80}Bi_{0.20}O_{3\text{-delta}}$ and $BaPb_{0.60}Bi_{0.40}O_{3\text{-delta}}$ with zero electrical resistivity at ~11 K, J. Alloys Compd. 815 (2020), 152460.

[35] L.F. Mattheiss, E.M. Gyorgy, D.W. Johnson, Superconductivity above 20 K in the Ba-K-Bi-O system, Phys. Rev. B Condens. Matter 37 (1988) 3745–3746.

[36] M. Zhang, M.A. Farid, H. Zhang, J.L. Sun, G.B. Li, F.H. Liao, J.H. Lin, Superconductivity of perovskite $Ba_{1-x}Y_x(Bi_{0.2}Pb_{0.8})O_{3-\delta}$, J. Supercond. Nov. Magnetism 30 (2017) 1705–1712.

[37] A. Firdous, X.G. Wang, M.A. Farid, M. Zhang, Y. Wang, J.L. Geng, J.L. Sun, G.B. Li, F.H. Liao, J.H. Lin, Superconductivity in perovskite $Ba_{0.85-x}La_xPr_{0.15}(Bi_{0.20}Pb_{0.80})O_{3-\delta}$, J. Supercond. Nov. Magnetism 32 (2019) 167–173.

[38] N.R. Khasanova, F. Izumi, T. Kamiyama, K. Yoshida, A. Yamamoto, S. Tajima, Crystal structure of the $(K_{0.87}Bi_{0.13})BiO_3$ superconductor, J. Solid State Chem. 144 (1999) 205–208.

[39] S.M. Kazakov, C. Chaillout, P. Bordet, J.J. Capponi, M. Nunez-Regueiro, A. Rysak, J.L. Tholence, P.G. Radaelli, S.N. Putilin, E.V. Antipov, Discovery of a second family of bismuth-oxide-based superconductors, Nature 390 (1997) 148–150.

[40] N.R. Khasanova, K. Yoshida, A. Yamamoto, S. Tajima, Extended range of superconducting bismuthates $K_{1-x}A_xBiO_3$ (A=La, Bi, and Ca), Phys. C (Amsterdam, Neth.): Supercond. Appl. 356 (2001) 12–22.

[41] M.H.K. Rubel, T. Takei, N. Kumada, M.M. Ali, A. Miura, K. Tadanaga, K. Oka, M. Azuma, M. Yashima, K. Fujii, E. Magome, C. Moriyoshi, Y. Kuroiwa, J.R. Hester, M. Aydeev, Hydrothermal synthesis, crystal structure, and superconductivity of a double-perovskite Bi oxide, Chem. Mater. 28 (2016) 459–465.

[42] Z. Iqbal, G.H. Kwei, B.L. Ramakrishna, E.W. Ong, Structure and bulk superconductivity of $BaPb_{0.5}Bi_{0.25}Tl_{0.25}O_{3-\delta}$, Phys. C (Amsterdam, Neth.): Supercond. Appl. 167 (1990) 369–374.

[43] M.H.K. Rubel, T. Takei, N. Kumada, M.M. Ali, A. Miura, K. Tadanaga, K. Oka, M. Azuma, E. Magomae, C. Moriyoshi, Y. Kuroiwa, Hydrothermal synthesis of a new Bi-based $(Ba_{0.82}K_{0.18})(Bi_{0.53}Pb_{0.47})O_3$ superconductor, J. Alloys Compd. 634 (2015) 208–214.

[44] M.H.K. Rubel, T. Takei, N. Kumada, M.M. Ali, A. Miura, K. Tadanaga, K. Oka, M. Azuma, E. Magome, C. Moriyoshi, Y. Kuroiwa, Hydrothermal synthesis, structure, and superconductivity of simple cubic perovskite $(Ba_{0.62}K_{0.38})(Bi_{0.92}Mg_{0.08})O_3$ with Tc similar to 30 K, Inorg. Chem. 56 (2017) 3174–3181.

[45] R.J. Cava, B. Batlogg, G.P. Espinosa, A.P. Ramirez, J.J. Krajewski, W. Peck, L. W. Rupp, A.S. Cooper, Superconductivity at 3.5 K in $BaPb_{0.75}Sb_{0.25}O_3$ - why is Tc so low, Nature 339 (1989) 291–293.

[46] X.D. Zheng, L. Zhang, X.G. Wang, Y.G. Qing, J. Chen, Y.D. Wu, S.H. Deng, L.H. He, F.H. Liao, Y. Wang, J.L. Geng, J.L. Sun, G.B. Li, L.J. Liu, J.H. Lin, Synthesis, structure, and superconductivity of B-site doped perovskite bismuth lead oxide with indium, Inorg. Chem. Front. 7 (19) (2020) 3561–3570.

[47] H.M. Rietveld, A profile refinement method for nuclear and magnetic structures, J. Appl. Crystallogr. 2 (1969) 65–71.

[48] A.C. Larson, R.B. von Dreele, Report LAUR 86–748, Los Alamos National Laboratory, Los Alamos, NM, 1985.

[49] S.M. Antao, I. Hassan, $BaCO_3$: high-temperature crystal structures and the *Pmcn-R3m* phase transition at 811°C, Phys. Chem. Miner. 34 (2007) 573–580.

[50] V.G. Tsirelson, A.S. Avilov, Y.A. Abramov, E.L. Belokoneva, R. Kitaneh, D. Feil, X-Ray and electron diffraction study of MgO, Acta Crystallogr. B54 (1998) 8–17.

[51] L. Vegard, The constitution of the mixed crystals and the filling of space of the atoms, Eur. Phys. J. A. 5 (1921) 17–26.

[52] L. Vegard, X-rays in the service of research on matter, Z. für Kristallogr. - Cryst. Mater. 67 (1928) 239–259.

[53] H. Wang, C.H. Wang, G.B. Li, T.N. Jin, F.H. Liao, J.H. Lin, Synthesis, Structure, and characterization of the series $BaBi_{1-x}Ta_xO_3$ ($0 <= x <= 0.5$), Inorg. Chem. 49 (2010) 5262–5270.

[54] I.C. Kaya, V. Kalem, H. Akyildiz, Hydrothermal synthesis of pseudocubic $BaTiO_3$ nanoparticles using TiO_2 nanofibers: study on photocatalytic and dielectric properties, Int. J. Appl. Ceram. Technol. 16 (2019) 1557–1569.

[55] X. Ma, A. Firdous, L. Zhang, S.J. Wu, J.X. Zhang, L.J. Liu, Y. Wang, J.L. Geng, J. L. Sun, G.B. Li, F.H. Liao, J.H. Lin, Superconductivity in perovskite $Ba_{1-x}K_xBi_{0.30}Pb_{0.70}O_{3-\delta}$, ChemistrySelect 4 (2019) 3135–3139.

[56] M.A. Hamza, A.N. El-Shazly, N.K. Allam, Facile template-free one-pot room-temperature synthesis of novel m-$Bi(OH)CrO_4$ microspheres, Mater. Lett. 262 (2020), 127188.

[57] Z.M. Yang, D.Z. Zhang, H.N. Chen, MOF-Derived indium oxide hollow microtubes/MoS_2 nanoparticles for NO_2 gas, Sens. Actuators, B 300 (2019), 127037.

[58] J. Hu, Y. Liang, Y. Sun, Z. Zhao, M. Zhang, P. Li, W. Zhang, Y. Chen, S. Zhuiykov, Highly sensitive NO_2 detection on ppb level by devices based on Pd-loaded In_2O_3 hierarchical microstructures, Sens. Actuators, B 252 (2017) 116–126.

[59] N.L. Jones, J.B. Parise, R.B. Flippen, A.W. Sleight, Superconductivity at 34 K in the K/Ba/Bi/O system, J. Solid State Chem. 78 (1989) 319.

[60] S. Pei, J.D. Jorgensen, B. Dabrowski, D.G. Hinks, D.R. Richards, A.W. Mitchell, Structural phase diagram of the $Ba_{1-x}K_xBiO_3$ system, Phys. Rev. B 41 (1990) 4126.

[61] D. Szczesniak, A.Z. Kaczmarek, E.A. Drzazga, K.A. Szewczyk, R. Szczesniak, On the superconducting state in $Ba_{0.6}K_{0.4}BiO_3$ perovskite oxide, Physica B 536 (2018) 676.

[62] Z.F. Wu, K. Wang, S.G. Yang, Z.H. Wang, Phase diagram and flux pinning in Bi-doping $BaPbO_3$ compounds, J. Alloys Compd. 750 (2018) 436.